RP Current Trends In Engineering And Technology
Vol. 3, No. 3 (July – September 2024) pp. 46–53
e-ISSN: 2583-5491

RESEARCH PLATEAU PUBLISHERS

Cite this article: N. Singh, High capacity hydrogen storage using magnesium aluminate nanoparticles: sol-gel synthesis, characterization, and electrochemical analysis, *RP Cur. Tr. Eng. Tech*. **3** (2024) 46–53.

Original Research Article

High-capacity hydrogen storage using magnesium aluminate nanoparticles: sol-gel synthesis, characterization, and electrochemical analysis

Navneet Singh*
Department of Physics, Rajiv Gandhi Government College for Women, Bhiwani – 127021, Haryana, India
*Corresponding author, E-mail: ndhanda16@gmail.com

ARTICLE HISTORY
Received: 30 July 2024
Revised: 02 Sept. 2024
Accepted: 04 Sept. 2024
Published online: 07 Sept. 2024

KEYWORDS
Hydrogen storage; Magnesium aluminate; Debye-Scherrer analysis; Nanoparticles; XRD; FTIR; DRS; EDS; FESEM; Chronopotentiometry (CP) method.

ABSTRACT
We used stearic acid as a capping ingredient in a sol-gel process to create magnesium aluminate ($MgAl_2O_4$) spinel nanoparticles. Nanoparticles with an average crystallite size of 12 nm were synthesized by calcination at 900°C for 4 hours, as verified by X-ray diffraction (XRD) data and Debye-Scherrer analysis. According to a research using Diffuse Reflectance Spectroscopy (DRS), the optical band gap was 2.84 eV. According to our Brunauer-Emmett-Teller (BET) analysis, the nanoparticles' average pore size was 20.2 nm. The resulting powders were characterized using a range of methods, such as vibrating sample magnetometry, energy-dispersive X-ray spectroscopy (EDS), field emission scanning electron microscopy (FESEM), and Fourier transform infrared (FTIR) spectroscopy. For electrochemical studies, we employed the Chronopotentiometry (CP) method. According to electrochemical studies, $MgAl_2O_4$ spinel nanoparticles have a noteworthy 4000 mAh/g hydrogen storage capacity, which makes them attractive options for hydrogen storage applications. The outstanding synthesis, thorough characterization, and remarkable electrochemical performance of $MgAl_2O_4$ spinel nanoparticles are highlighted in this extensive work, solidifying their status as useful materials for advancing hydrogen storage systems.

1. Introduction

Concerns over the planet's future have grown as a result of the fast increase in the use of fossil fuels and the expansion of human society [1]. Moreover, the type and quantity of energy used affects human activities now and in the future. Therefore, utilizing clean fuels like hydrogen, green energies, and renewable energy sources is a safe and efficient way to lessen environmental pollution [2]. Research on hydrogen synthesis utilizing renewable energy sources is now underway in order to achieve this aim [3]. Because of its high energy content, efficiency in energy conversion, and renewability, hydrogen has the potential to be employed as an energy carrier. Steel production, hybrid automobiles, engine fuel, and fuel cells are just a few of the sectors that might employ hydrogen [5, 6]. The lightest and most prevalent element in the universe is hydrogen. Hydrogen has a higher energy density per volume than other fossil fuels, such as gasoline, and is frequently kept in massive tanks [7]. Effective, secure, and economical storage of hydrogen is required.

There are two ways to store hydrogen: chemically and physically. Physical absorption is a common method of storing hydrogen in nanomaterials [8]. Transition mixed metal oxides [9], polymers [10], metal-organic frameworks (MOFs) [11], and graphene nanocomposites [12] are among the materials that may store hydrogen. Because of their small size for absorbing and releasing hydrogen molecules, reversible storage potential, high surface-to-volume ratio, and structural stability during physicochemical interactions, nanoparticles perform better in hydrogen storage than other materials [13]. One of the safest and most effective methods is to store hydrogen in solid-state materials [14].

Numerous spinel oxides, such as $NiCr_2O_4$ [15], $NiAl_2O_4$ [16], and $MgCr_2O_4$ [17], have been created via a variety of techniques. Spinels like $BaAl_2O_4$ and $CoAl_2O_4$ have been demonstrated in earlier research to be capable of storing hydrogen [18, 19].

Magnesium aluminate spinel ($MgAl_2O_4$) has drawn attention from researchers due to its remarkable physicochemical properties, which include mechanical, optical, dielectric, thermal, and electrochemical properties. For energy storage applications, $MgAl_2O_4$ has been extensively studied in a range of forms, such as nanoparticles and nanocomposites [20, 21, 22]. Moreover, new nanostructures that may be useful for hydrogen storage are created when $MgAl_2O_4$ is combined with other substances, such as metal oxides [23]. Magnesium aluminate oxide's wide specific surface area and porous structure, which lead to the establishment of many active sites for hydrogen absorption, are among its most important advantages over other hydrogen storage materials [24]. Among the many uses for magnesium aluminate are supercapacitors [21], catalysts [27], humidity sensors [26], and hydrogen production [25]. Numerous methods, such as sol-gel [28], co-precipitation [29], hydrothermal [27], solution combustion [30], and solid-state [31], have been used to synthesize $MgAl_2O_4$.

Compared to alternative techniques, the sol-gel method of synthesizing magnesium aluminate spinel ($MgAl_2O_4$) offers

several advantages. This method minimizes impurities in the finished product and uses pure metallic precursors to attain high purity. Sol-gel-derived $MgAl_2O_4$ also frequently demands lower sintering temperatures, which improves energy efficiency without sacrificing material properties. Additionally, the method permits fine dopant control, which permits the uniform addition of ions to modify material properties for particular uses [15, 32, 33].

Stearic acid was utilized as a capping agent for the first time, and $MgAl_2O_4$ spinel nanoparticles were synthesized using a sol-gel process. Because of its lengthy carbon chain, stearic acid effectively prevents the agglomeration of nanoparticles. Numerous methods, including XRD, FTIR, FESEM, EDS, DRS, VSM, and BET, were used to study magnesium aluminate. Investigations were conducted on the hydrogen storage capacity as well as a number of attributes, including copper sheet surface, cycle number, and current intensity. According to the study, $MgAl_2O_4$ nanoparticles might be a good material for storing hydrogen.

2. Experimental

2.1 Materials and methods

Merck provided stearic acid ($C_{18}H_{36}O_2$), magnesium acetate ($Mg(OAc)_2{\cdot}4H_2O$), and 99.9% pure aluminum nitrate ($Al(NO_3)_3{\cdot}9H_2O$). In order to investigate the structural evolution and crystallization of the sample, the XRD patterns of $MgAl_2O_4$ nanoparticles were examined using a Model PTS 3003 SEIFERT diffractometer with Cu Kα radiation (λ = 1.54 Å) and in the 2θ range from 10° to 80°. An MB100 (BOMEM) spectrophotometer and a KBr pellet were used to get the FTIR spectra of $MgAl_2O_4$ nanoparticles. The size distribution and surface morphology of the samples were examined using a FESEM. The energy dispersive spectrometry (EDS) was evaluated using the Philips EM208. A vibrating sample magnetometer was used to examine the sample's magnetic properties. Using UV absorption spectra at 300–500 nm, the sample's band gap was assessed. N_2 adsorption/desorption tests were performed using an ASAP-2010 analyzer to determine the catalysts' Brunauer-Emmett-Teller (BET) specific surface areas. Using the SAMA 500 electro-analyzer apparatus, the chronopotentiometry method was employed in Iran to ascertain a sample's discharge capacity (hydrogen storage capacity).

2.2 Preparation of $MgAl_2O_4$ spinel nanoparticles

Using magnesium acetate as the cation source, aluminum nitrate as the cation source, and stearic acid as a capping agent, $MgAl_2O_4$ spinel nanoparticles (NPs) were synthesized via the sol-gel technique. Start by melting 10 mmol of stearic acid at 73°C in a beaker. Next, distilled water (pH=4) was used to dissolve 1 mmol magnesium acetate and 2 mmol aluminum nitrate. Stearic acid was mixed with metallic ion solutions and stirred at 65 to 85 degrees Celsius to form a viscous gel. The gel was allowed to cool to room temperature before being dried for 24 hours at 85°C in an electric oven. A homogenous sol is created during this period when metal cations diffuse from the aqueous to the organic phases. The $MgAl_2O_4$ spinel nanoparticles were synthesized by calcining the dry gel for four hours at 700–900°C. $MgAl_2O_4$ spinel NPs were synthesized in Scheme 1 for four hours at 700 and 900°C (see Table 1).

Table 1: The basic constituents of spinel NPs of $MgAl_2O_4$ at 900 °C.

Element	Mg	Al	O	Total
W (%)	19.83	48.31	31.86	100
Mole fraction	0.15	0.3	0.55	1

2.3 Electrochemical hydrogen storage

One useful technique for calculating hydrogen storage capacitance is chronopotentiometry. Ag/AgCl, Pt, and Cu-$MgAl_2O_4$ are the electrodes in this electrochemical cell, respectively. A 6 M potassium hydroxide aqueous solution serves as the electrolyte. The potential differences between the working and Ag/AgCl (reference) electrodes are computed in this system by delivering a current intensity of ±1 mA between the counter (anode) and working (cathode) electrodes. A thin copper sheet was used as a Cu/$MgAl_2O_4$ substrate in order to create a Cu-$MgAl_2O_4$ electrode. For ten minutes, magnesium aluminum oxide powder is sonicated in ethanol. $MgAl_2O_4$ powder is applied to a copper sheet (1 cm^2) at 100°C [13].

3. Results and discussion

3.1 XRD analysis

In the 2θ range of 10º to 80º, Figure 1(a) displays XRD diffractograms of $MgAl_2O_4$ spinel nanoparticles that were calcined at 700 and 900°C for four hours. The XRD pattern of $MgAl_2O_4$ calcined at 700°C is displayed in Figure 1(a), with faint, low-intensity peaks. The fundamental structure of the nanoparticles is developing at 700°C, but crystals have not yet reached their full size. Wider diffraction peaks result from crystals growing larger when the temperature is raised to 900°C. Crystal planes (111), (220), (311), (400), (422), (511), and (440) are represented by diffraction peaks at 2θ values of 19º, 31º, 37º, 45º, 56º, 59.6º, and 65.5º. According to the study, the cubic crystal structure of $MgAl_2O_4$ (JCPDS-01-071-2499) has space group Fd-3m and lattice parameters $a = b = c =$ 8.05Å. No pollutants, such as MgO or Al_2O_3, were found. Using the Debye-Scherrer relation (Eq. 1), the average crystallite size of $MgAl_2O_4$ spinel nanoparticles calcined at 900°C for 4 hours was ascertained from the XRD diffractogram [34].

$$D = k\lambda\beta\cos\theta \quad (1)$$

where D is the mean particle diameter, λ is the wavelength (0.15418 nm), θ is the diffraction angle, β is the breadth of the XRD peak at half height, and k is a shape factor of around 0.9 for spherical-shaped nanoparticles. The linear fit of Eq. (1) to the plot of cosθ vs 1/β in Figure 1(b) was used to calculate the average crystallite size. Higher temperatures encourage the development of crystals, and the average crystal size was calculated to be 12 nm [35]. In order to evaluate the impact of the lattice on strain and peak broadening, the Williamson-Hall (W-H) relation was utilized [36, 37] (Eq. 2).

$$B\cos\theta = k\lambda D + 4\varepsilon\sin\theta \quad (2)$$

where D is the average crystallite size and ε is the lattice strain. Figure 1(c) illustrates how the lattice strain and crystallite size were determined using the Williamson-Hall plot. The fit of Eq. (2) to the β cosθ vs. 4 sinθ plot is displayed in Figure 1(c). The average crystallite size and lattice strain were estimated using the graph's intercept and slope, yielding

values of 17.35 nm and 296 × 10^{-5}, respectively. Compared to the Debay-Scherrer equation, the Williamson-Hall equation produces a somewhat larger crystallite size. The strain impact as calculated by the Williamson-Hall equation [38] (Figure 2) may be the cause of this disparity.

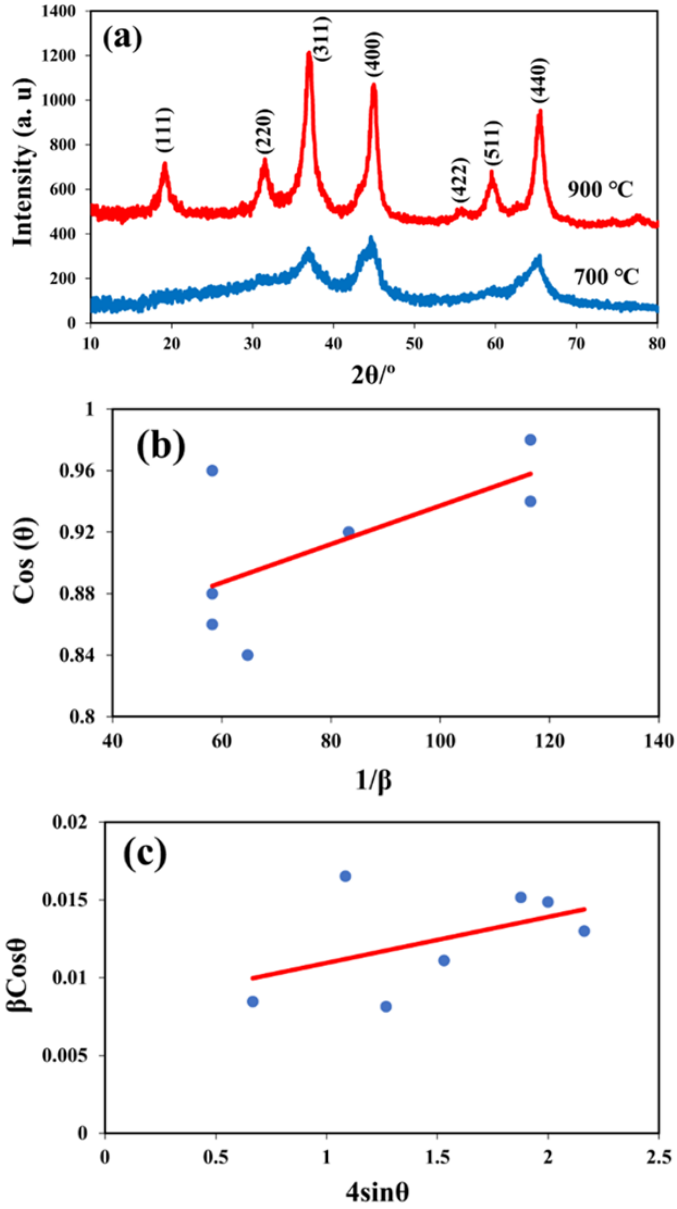

Figure 1: (a) XRD diffractogram of synthesized $MgAl_2O_4$; (b) Debye–Scherrer plot; (c) Williamson-Hall plot.

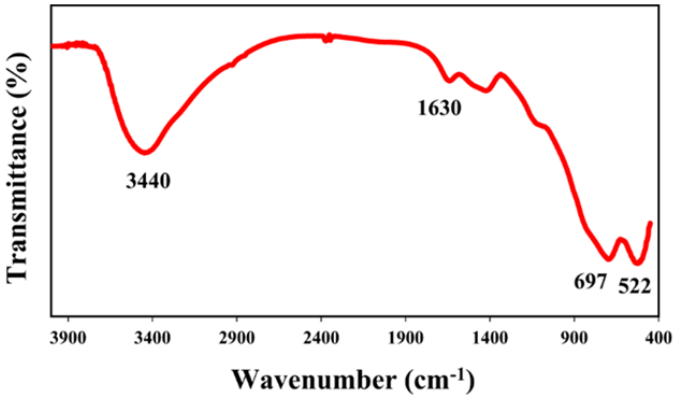

Figure 2: FTIR analysis of $MgAl_2O_4$ spinel nanoparticles synthesized at 900°C.

3.2 FTIR spectroscopy

The FT-IR spectroscopy results for $MgAl_2O_4$ spinel NPs at 900°C are shown in Figure 2. Metal-oxygen bond vibrations, such as Mg-O stretching in the lattice and Al-O stretching in the AlO_6 group, are responsible for two absorption bonds at 522-697 cm^{-1} [28, 39]. Bending (H-O-H) is indicated by the vibration bond at 1630 cm^{-1}, whereas the OH group is represented by the vibration band at around 3440 cm^{-1} [40].

3.3 FESEM and energy dispersive X-ray (EDS)

The surface morphology of $MgAl_2O_4$ spinel NPs calcined at 900 °C was investigated using FESEM analysis. Figures 3 (a, b) display the sample's FESEM images. The powder sample had a homogeneous structure and formed uniform spherical shapes. Additionally, Image J was used to analyze the FESEM pictures of $MgAl_2O_4$ spinel nanoparticles [39]. The sample's histogram plot is displayed in Figure 3(c). It was found that the average particle size was 25 nm. Figure 4 displays the $MgAl_2O_4$ spinel nanoparticles' EDX spectrum. The EDS results demonstrate the presence of impurity-free magnesium, aluminum, and oxygen components. The basic components of $MgAl_2O_4$ spinel NPs are displayed in Table 1 [41, 42].

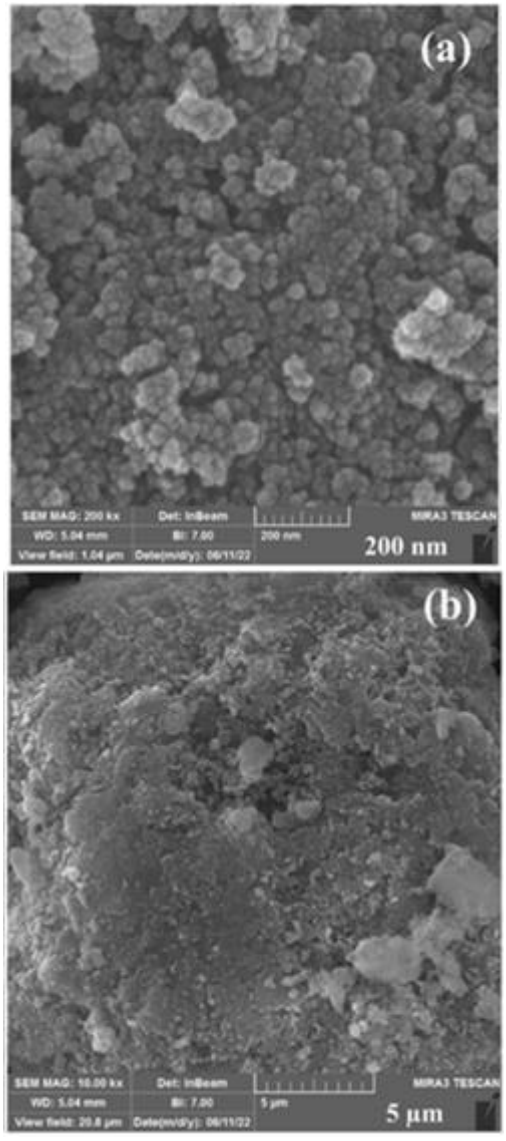

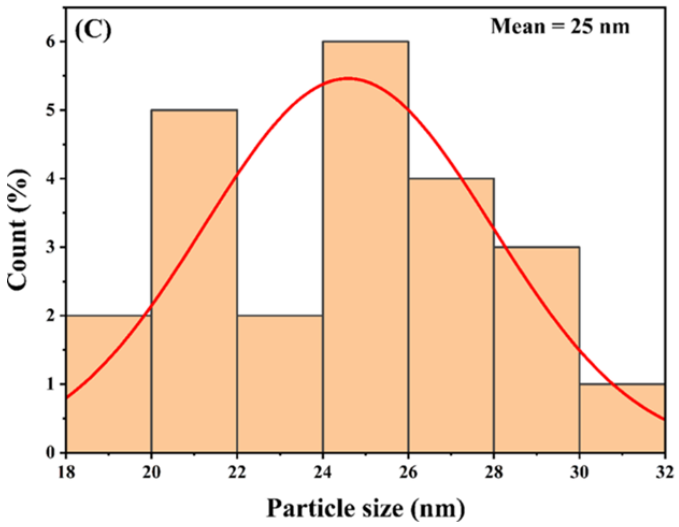

Figure 3: (a, b) Synthetic $MgAl_2O_4$ spinel NPs at 900 °C: FESEM pictures; (c) particle size distribution.

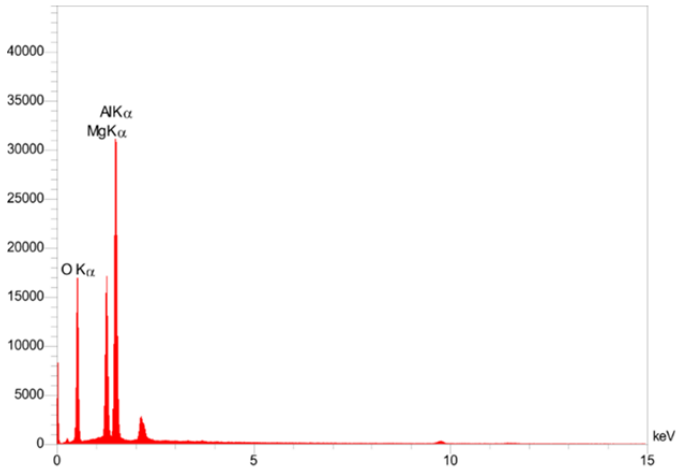

Figure 4: EDS spectrum of $MgAl_2O_4$ NPs at 900 °C.

3.4 Optical properties

Desired characteristics of semiconductors that affect their optoelectronic applications include the energy gap (E_g) and absorption coefficient. The UV-vis absorption spectrum of $MgAl_2O_4$ spinel NPs at 300–500 nm is displayed in Figures 5 (a, b). The charge transfer from O^{2-} to Al^{3+} may be the cause of the 380 nm absorption peak [43]. Tuac's relation (E_g) was used to compute the photon energy (E_g) (Eq. 3).

$$(\alpha h\nu)\, n = A\,(h\nu - E_g) \qquad (3)$$

where h is the Planck's constant ($6.62607004 \times 10^{-34}$ m^2kg/s), n is the transmission mode, ϋ is the frequency (Hz), α is the absorption coefficient, A is the energy independent constant, and E_g band gap energy (eV). A graph of $(\alpha h\ddot{u})^2$ values was plotted against the band gap energy (hϋ) axis in order to examine the band gap energy of the nanoparticle. The energy axis interruption was calculated by extrapolating the linear section of the absorption edge. The optical band gap of $MgAl_2O_4$ spinel nanoparticles is shown in Figure 5 (b). $MgAl_2O_4$ spinel nanoparticles were discovered to have a direct band gap of 2.84 eV [31]. According to earlier studies, the calcination temperature affects the optical reflectance of $MgAl_2O_4$ spinel nanoparticles [44]. The size of the $MgAl_2O_4$ crystallites increases when the calcination temperature climbs over 800 °C, which lowers the band gap energy. In other words, the cubic crystal structure of $MgAl_2O_4$ spinel NPs is responsible for their optical reflectance properties. The development of defect states between the valence and conduction bands could be the cause of the drop in bandgap energy [45]. $MgAl_2O_4$ spinel NPs may therefore function as a photocatalyst in addition to a semiconductor.

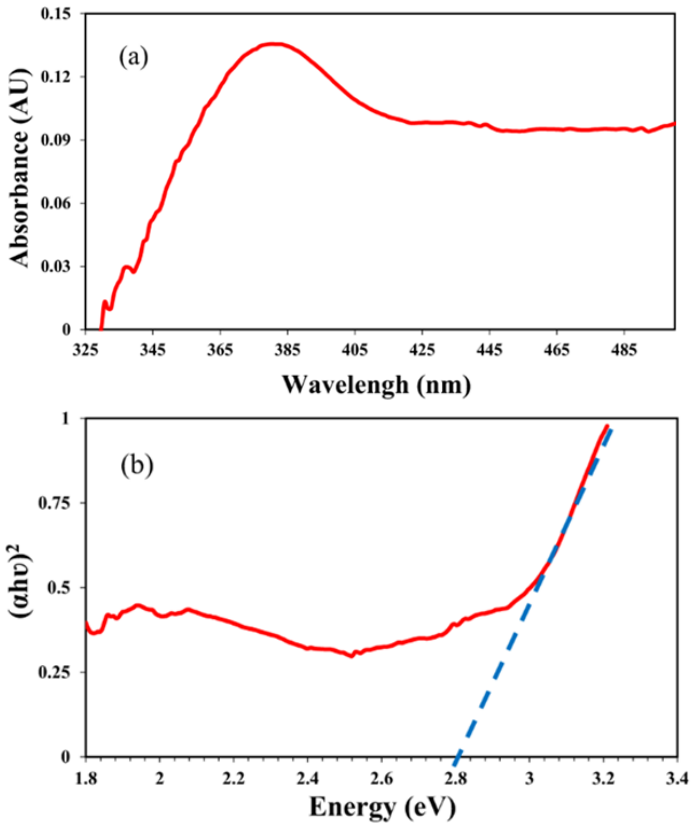

Figure 5: (a) Synthesized $MgAl_2O_4$ NPs' DRS at 900°C. (b) Synthesized $MgAl_2O_4$ NPs' optical band gap at 900°C.

3.5 VSM studies

It has been studied how $MgAl_2O_4$ spinel NPs behave magnetically (Figure 6). At room temperature, the magnetic properties of the material were investigated. The ferromagnetic properties of $MgAl_2O_4$ spinel NPs are shown by the M-H curve. $MgAl_2O_4$ spinel NPs' ferromagnetic characteristics have already been reported [46]. The values of the coercivity field (H_c), remanence magnetization (M_r), and saturation magnetization (M_s) were around 200 O_e, 0.0244 emu/g, and 0.0154 emu/g, respectively. It was found that the remanence ratio (MR/MS) was around 1.584. Their capacity to magnetize strongly in the presence of an external field is indicated by their saturation magnetization (M_s) of 0.0154 emu/g. The H_c of 200 O_e demonstrates $MgAl_2O_4$ resistance to demagnetization, however this M_r result shows strong magnetic memory after the field is removed. Its potential for application in data storage and magnetic devices is demonstrated by the value of 1.584, which highlights the (M_r/M_s) capacity to retain magnetization. Magnetic ions in the crystal structure of normal spinel, sometimes referred to as cubic spinel, can cause it to exhibit ferromagnetic activity. The chemical formula for this mineral is AB_2O_4, where A and B stand for different metal cations. The alignment of these cations' magnetic moments within the crystal lattice produces ferromagnetism. Exchange interactions

between magnetic ions that occupy both the A and B sites encourage parallel alignment of their magnetic moments. Saturation magnetization is the outcome of the magnetic moments aligning with the applied magnetic field. Groups of atomic magnetic moments aligning in the same direction can be observed as magnetic domains in bulk normal spinel. The exact combination of magnetic ions and how they are arranged in the lattice, along with temperature, determine the ferromagnetism of each typical spinel compound. The behavior of magnetic moments within the crystal structure and quantum mechanical interactions are the causes of ferromagnetism in normal spinel.

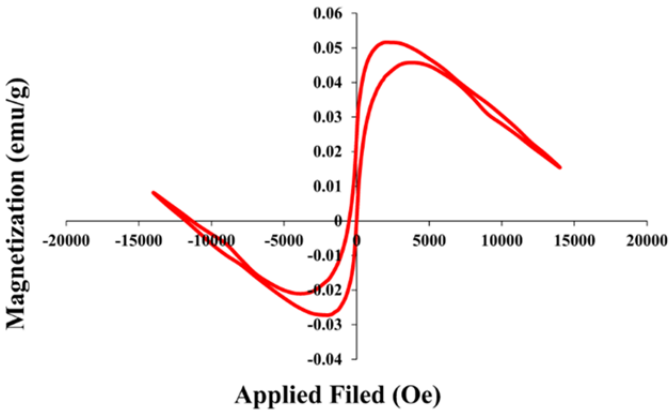

Figure 6: M-H curve of synthesized $MgAl_2O_4$ NPs at 900°C.

3.6 BET technique

The BET-BJH method was used to determine the specific surface area of $MgAl_2O_4$ spinel NPs at 900 °C. The results are displayed in Figures 7 (a and b). Class IV can be described in adsorption isotherms with hysteresis loops, according to the N_2 adsorption/desorption and IUPAC categorization [35].

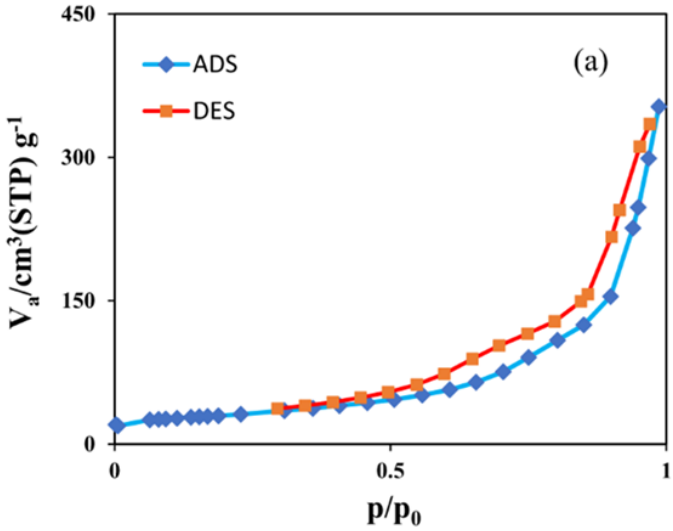

Mesoporous $MgAl_2O_4$ spinel nanoparticles display H_3-type hysteresis. A substantial adsorption capability is shown by the specific surface area of 108.1 m²/g, which indicates a sizable surface area available for interactions with hydrogen molecules. The material is suitable for real-world applications like fuel cells and transportation because of its pore volume of 0.5459 cm³/g, which shows that it can store significant volumes of hydrogen gas. The material's pore structure, which is essential for hydrogen mobility and accessibility, is revealed by the average pore size of 20.2 nm. Different masses of hydrogen can permeate into and out of the material due to the different pore sizes of the nanoparticles. According to the BET results, the material's significant specific surface area, pore volume, and mean pore size demonstrate its potential for gas adsorption and storage, especially with regard to hydrogen. For applications that require a consistent and unique nanoparticle structure, the FESEM data provide visual confirmation of the size, shape, and homogeneity of the particles, which may be essential.

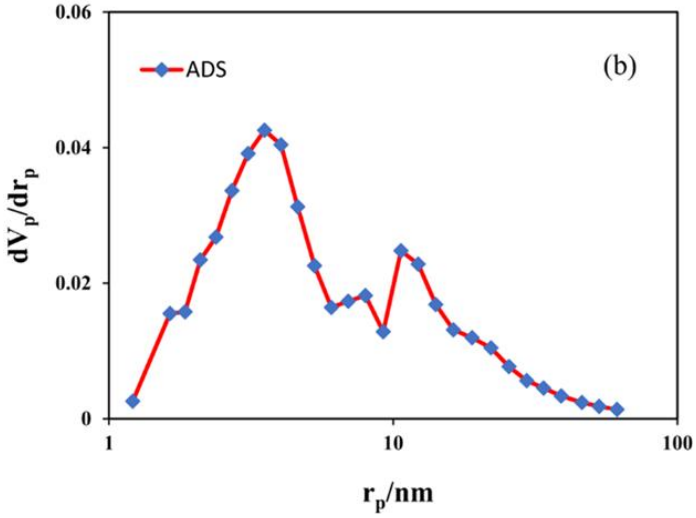

Figure 7: (a) N_2 adsorption-desorption isotherms, and (b) pore size distributions of the prepared sample at 900°C.

3.7 Hydrogen storage capacity

The discharge capacity of copper foam without $MgAl_2O_4$ presence is about equivalent to 3 mAh/g, as shown in Figure 8. The discharge characteristics of the Cu-$MgAl_2O_4$ electrode after five cycles at a constant current of 1 mA are shown in Figure 9. This figure also shows that the Cu-$MgAl_2O_4$ electrode's capacity may be impacted by its placement in an alkaline medium. According to Volmer, Tafel, and Heyrovsky [47], electrochemical hydrogen absorption processes take place during three reactions. A 6 M KOH mixture mixed in deionized water (a proton source) was used to create the electrolyte solution. Hydrogen atoms are created when water breaks down (Eq. 4). The electrolyte separates around the working electrode during the charging process (Volmer reaction), and hydrogen is adsorbed on the surface of the $MgAl_2O_4$ nanoparticles (Eq. 5).

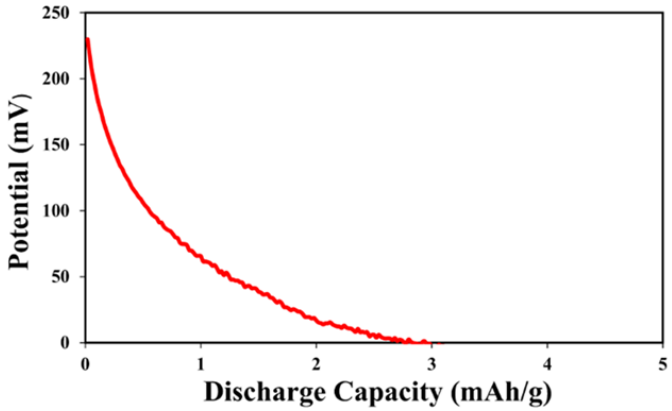

Figure 8: The discharge capacity of copper foam without attendance $MgAl_2O_4$.

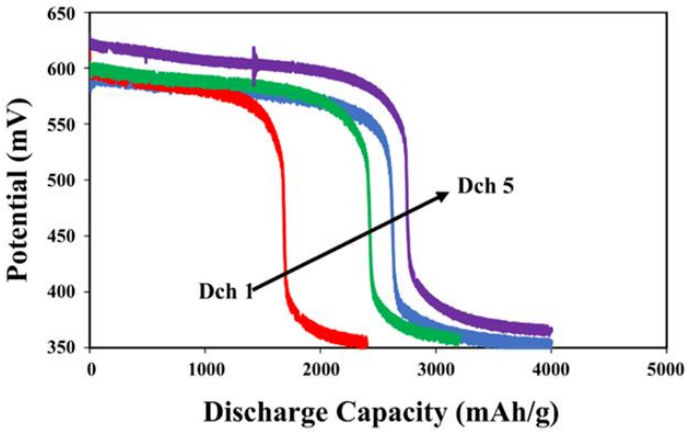

Figure 9: The discharge properties of the Cu- $MgAl_2O_4$ electrode over the 5 cycles under a current constant 1 mA.

$$H_2O + e^- \rightleftarrows H + OH^- \quad (4)$$

$$MgAl_2O_4 + H_2O + e^- \rightleftarrows (MgAl_2O_4{-}H_{ads}) + OH^- \quad (5)$$

Subsurface hydrogen (H_{ss}) is created when hydrogen atoms adsorb onto the working electrode surface and H_2O is reduced to hydroxyl ions, according to the Volmer.

$$MgAl_2O_4{-}H_{ads} \rightleftarrows MgAl_2O_4{-}H_{ss} \quad (6)$$

Subsurface hydrogen atoms (H_{ss}) then disperse as hydrogen that has been bulk-absorbed (H_{abs}).

$$MgAl_2O_4{-}H_{ss} \rightleftarrows MgAl_2O_4{-}H_{abs} \quad (7)$$

The migration of adsorbed *H* (H_{ads}) into the $MgAl_2O_4$ network is caused by a rise in surface accumulated hydrogen. An electron is released when the absorbed hydrogen atoms are desorbed from the working electrode's surface and converted back into water during the discharge process, which happens in the opposite direction from the charging process. One kind of physical adsorption is the adsorption of hydrogen atoms on the Cu-$MgAl_2O_4$ (cathode) surface [48]. After five cycles, the discharge capacity increased from 2380 mAh/g in the first cycle to 4000 mAh/g.The surface-to-volume ratio of $MgAl_2O_4$ spinel nanoparticles, the pore distribution, and the creation of more active sites for hydrogen desorption/absorption on the working electrode surface are likely responsible for the increase in discharge capacity. [49]. Gaseous hydrogen (H_2) is created if the energy required for hydrogen absorption is less than the energy released, according to the physical adsorption equations for electrochemical hydrogen storage, such as the Heyrovsky process (Eq. 11) and the sidewise Tafel reaction (Eqs. 9, 10).

$$MgAl_2O_4{-}H_{ads} + MgAl_2O_4{-}H_{ads} \rightleftarrows 2MgAl_2O_4 + H_2\,(g) \quad (8)$$

$$H + H \rightleftarrows H_2 \quad (9)$$

$$MgAl_2O_4{-}H_{ads} + H_2O + e^- \rightleftarrows MgAl_2O_4 + H_2(g) + OH^- \quad (10)$$

The cycling performance of the $MgAl_2O_4$ nanoparticles at a steady current of 1 mA is displayed in Figure 10. The discharge capacity may be used to determine how much hydrogen is stored in the working electrode. Using Eq. 11 [50], the electrodes' charge/discharge curves may be used to determine the storage capacity (SC).

$$\text{Storage Capacity (SC)} = [\text{Time (h)} \times \text{Current (mA)}]/\ \text{Active Mass (g)} \quad (11)$$

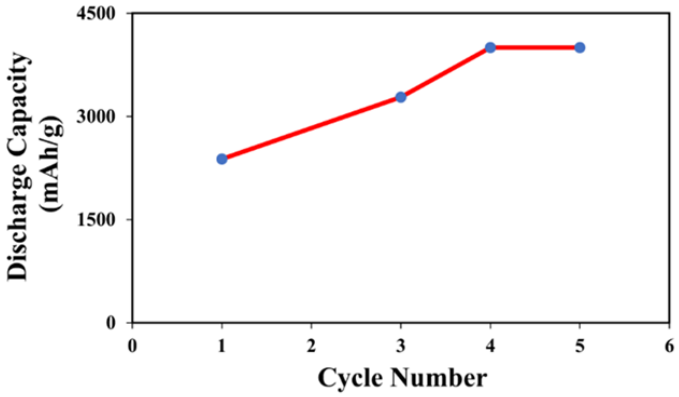

Figure 10: Cycling effect of Cu-$MgAl_2O_4$ electrodes on the amount of storage capacity at 1 mA.

The $MgAl_2O_4$ spinel nanoparticles' cheap cost, acceptable electrochemical discharge capacity, and fewer cycle numbers make them appropriate. $MgAl_2O_4$ spinel nanoparticles and the previously published nanomaterials are contrasted in Table 2.

Table 2: Comparison of the hydrogen discharge capacity of different nanomaterials.

Sample	Number of Cycle	Discharge Capacity ($mAhg^{-1}$)	Ref.
$MgMn_2O_4$	5	2000	[9]
$Ca_2Mn_3O_8/CaMn_3O_6$	95	105	[51]
Fe_3O_4/G	5	900	[52]
$MgAl_2O_4$	5	4000	Current Paper

3. Conclusions

In conclusion, stearic acid was used as a capping ingredient in the sol-gel technique to successfully create $MgAl_2O_4$ spinel nanoparticles (NPs) at 900 °C. According to the obtained data, a mesoporous structure was linked to an average crystallite size of about 12 nm and a specific surface area of 108.1 m^2g^{-1}. With a constant tiny, homogeneous, and spherical shape and no impurities, the EDS and FESEM tests verified the purity of the obtained $MgAl_2O_4$ spinel NPs. Additionally, Diffuse Reflectance Spectroscopy (DRS) indicates that the optical band gap, which was determined to be 2.84 eV, is within the range that indicates effective photo-catalytic action. The research conducted by the Vibrating Sample Magnetometer (VSM) revealed ferromagnetic properties in the nanoparticles. The unique structure and characteristics of $MgAl_2O_4$ spinel nanoparticles make them promising for use in hydrogen energy storage. The promise of the nanoparticles as a viable option for hydrogen storage applications was confirmed by their remarkable maximum discharge capacity of 4000 mAh/g.

References

[1] K. Bilen, O. Ozyurt, K. Bakırcı, S. Karslı, S. Erdogan, M. Yılmaz, O. Comaklı, Energy production, consumption, and environmental pollution for sustainable development: a case study in Turkey,*Renew. Sustain. Energy Rev.* **12** (2008) 1529–1561.

[2] S. Sharma, A. Agarwal, A. Jain, Significance of hydrogen as economic and environmentally friendly fuel, *Energies* **14** (2021) 7389.

[3] F. Qureshi, M. Yusuf, H. Kamyab, S. Zaidi, M. Junaid Khalil, M. Arham Khan, M. Azad Alam, F. Masood, L. Bazli, S. Chelliapan, B. Abdullah, Current trends in hydrogen production, storage and applications in India: a review, *Sustain. Energy Technol. Assessments* **53** (2022) 102677.

[4] M.F. Orhan, B.S. Babu, Investigation of an integrated hydrogen production system based on nuclear and renewable energy sources: Comparative evaluation of hydrogen production options with a regenerative fuel cell system, *Energy* **88** (2015) 801–820.

[5] W. Liu, H. Zuo, J. Wang, Q. Xue, B. Ren, F. Yang, The production and application of hydrogen in steel industry, *Int. J. Hydrogen Energy* **46** (2021) 10548–10569.

[6] L. Bartolucci, E. Cennamo, S. Cordiner, V. Mulone, F. Pasqualini, M.A. Boot, Digital twin of a hydrogen fuel cell hybrid electric vehicle: effect of the control strategy on energy efficiency, *Int. J. Hydrogen Energy* **48** (2023) 20971–20985.

[7] B.C. Tashie-Lewis, S.G. Nnabuife, Hydrogen production, distribution, storage and power conversion in a hydrogen economy—a technology review, *Chem. Eng. J. Adv.* **8** (2021) 100172.

[8] Y.P. Chen, S. Bashir, J.L. Liu, Nanostructured materials for next-generation energy storage and conversion, Springer, Berlin, Heidelberg (2017) pp. 117–142.

[9] A. Eslami, S.A. Lachini, M. Shaterian, M. Karami, M. Enhessari, Synthesis, characterization, and hydrogen storage capacity of $MgMn_2O_4$ spinel nanostructures, *Inorg. Chem. Commun.* (2023) 110875.

[10] N. Mahato, H. Jang, A. Dhyani, S. Cho, Recent progress in conducting polymers for hydrogen storage and fuel cell applications, *Polymers* (Basel) **12** (2020) 2480.

[11] Y. Cao, H.A. Dhahad, S.G. Zare, N. Farouk, A.E. Anqi, A. Issakhov, A. Raise, Potential application of metal-organic frameworks (MOFs) for hydrogen storage: Simulation by artificial intelligent techniques, *Int. J. Hydrogen Energy* **46** (2021) 36336–36347.

[12] C.U. Deniz, H. Mert, C. Baykasoglu, Li-doped fullerene pillared graphene nanocomposites for enhancing hydrogen storage: a computational study, *Comput. Mater. Sci.* **186** (2021) 110023.

[13] T. Gholami, M. Salavati-Niasari, S. Varshoy, Electrochemical hydrogen storage capacity and optical properties of $NiAl_2O_4$/NiO nanocomposite synthesized by green method, *Int. J. Hydrogen Energy* **42** (2017) 5235–5245.

[14] E. Boateng, A. Chen, Recent advances in nanomaterial-based solid-state hydrogen storage, *Mater. Today Adv.* **6** (2020) 100022.

[15] M. Javed, A.A. Khan, J. Kazmi, M.A. Mohamed, M.N. Khan, M. Hussain, R. Bilkees, Dielectric relaxation and small polaron hopping transport in sol-gel-derived $NiCr_2O_4$ spinel chromite, *Mater. Res. Bull.* **138** (2021) 111242.

[16] Y. Iqbal, W.H. Shah, B. Khan, M. Javed, H. Ullah, N. Khan, A.R. Khan, G. Asghar, A. Safeen, Small polaron hopping transport mechanism, dielectric relaxation and electrical conduction in $NiAl_2O_4$ electro-ceramic spinel oxide, *Phys. Scr.* **98** (2023) 065951.

[17] M. Javed, A.A. Khan, M.S. Ahmed, S.N. Khisro, J. Kazmi, R. Bilkees, M.N. Khan, M.A. Mohamed, Temperature dependent impedance spectroscopy and electrical transport mechanism in sol-gel derived $MgCr_2O_4$ spinel oxide, *Phys. B: Condens. Matter* **599** (2020) 412377.

[18] T. Gholami, M. Salavati-Niasari, S. Varshoy, Investigation of the electrochemical hydrogen storage and photocatalytic properties of $CoAl_2O_4$ pigment: Green synthesis and characterization, *Int. J. Hydrogen Energy* **41** (2016) 9418–9426.

[19] A. Salehabadi, M. Salavati-Niasari, F. Sarrami, A. Karton, Sol-Gel auto-combustion synthesis and physicochemical properties of $BaAl_2O_4$ nanoparticles; electrochemical hydrogen storage performance and density functional theory, *Renew. Energy* **114** (2017) 1419–1426.

[20] I. Ganesh, A review on magnesium aluminate ($MgAl_2O_4$) spinel: synthesis, processing and applications, *Int. Mater. Rev.* **58** (2013) 63–112.

[21] M.W. Alam, V.G.D. Kumar, C.R. Ravikumar, S.C. Prashantha, H.C.A. Murthy, M.R.A. Kumar, Chromium (III) doped polycrystalline $MgAl_2O_4$ nanoparticles for photocatalytic and supercapacitor applications, *J. Phys. Chem. Solids* **161** (2022) 110491.

[22] F. Ullah, M.T. Qureshi, K. Sultana, M. Saleem, M. Al Elaimi, R. Abdel Hameed, S. ul Haq, H.S. Ismail, M.S. Anwar, Structural and dielectric studies of $MgAl_2O_4$–TiO_2 composites for energy storage applications, *Ceram. Int.* **47** (2021) 30665–30670.

[23] D-W. Zeng, S. Peng, C. Chen, J-M. Zeng, S. Zhang, H-Y. Zhang, R. Xiao, Nanostructured Fe_2O_3/$MgAl_2O_4$ material prepared by colloidal crystal templated sol–gel method for chemical looping with hydrogen storage, *Int. J. Hydrogen Energy* **41** (2016) 22711–22721.

[24] F. Wang, M. Luo, Q. Liu, C. Shao, Z. Yang, X. Liu, J. Guo, Preparation of Pt/$MgAl_2O_4$ decalin dehydrogenation catalyst for chemical hydrogen storage application, *Catal. Lett*. (2023) 1–15.

[25] C. Gómez-Solís, S.L. Peralta-Arriaga, L.M. Torres-Martínez, I. Juárez-Ramírez, L.A. Díaz-Torres, Photocatalytic activity of MAl_2O_4 (M = Mg, Sr and Ba) for hydrogen production, *Fuel* **188** (2017) 197–204.

[26] S. Das, M.L. Rahman, P.P. Mondal, P.L. Mahapatra, D. Saha, Screen-printed $MgAl_2O_4$ semi-thick film based highly sensitive and stable capacitive humidity sensor, *Ceram. Int.* **47** (2021) 33515–33524.

[27] X. Zhang, Hydrothermal synthesis and catalytic performance of high-surface-area mesoporous nanocrystallite $MgAl_2O_4$ as catalyst support, *Mater. Chem. Phys.* **116** (2009) 415–420.

[28] S.S. Milani, M.G. Kakroudi, N.P. Vafa, S. Rahro, F. Behboudi, Synthesis and characterization of $MgAl_2O_4$ spinel precursor sol prepared by inorganic salts, *Ceram. Int.* **47** (2021) 4813–4819.

[29] S. Nam, M. Lee, B-N. Kim, Y. Lee, S. Kang, Morphology controlled Co-precipitation method for nano structured transparent $MgAl_2O_4$, *Ceram. Int.* **43** (2017) 15352–15359.

[30] S.R. Ghosh, S. Mukherjee, S. Banerjee, Development of spinel magnesium aluminate by solution combustion route using thiourea and urea as, *Fuel J. Eng. Res.***17** (2020) 135–141.

[31] S. Mukherjee, Development of spinel magnesium aluminate by modified solid state process and its characterization, *Mater. Today Proc.* **67** (2022) 314–319.

[32] N. Bai, X. Liu, Z. Li, X. Ke, K. Zhang, Q. Wu, High-efficiency TiO2/ZnO nanocomposites photocatalysts by

sol–gel and hydrothermal methods, *J. Sol-Gel Sci. Technol.* **99** (2021) 92–100.
[33] A.A. Khan, M. Javed, A. Rauf Khan, Y. Iqbal, A. Majeed, S.Z. Hussain, S.K. Durrani, Influence of preparation method on structural, optical and magnetic properties of nickel ferrite nanoparticles, *Mater. Sci.* **35** (2017) 58–65.
[34] M. Enhessari, S.A. Lachini, $CuMn_2O_4$ nanostructures: facial synthesis, structural, magnetical, electrical characterization and activation energy calculation, *Int. J. Bio Inorg. Hybr. Nanomater.* **8** (2019) 39–45.
[35] S. SanjabiA. Obeydavi, Synthesis and characterization of nanocrystalline $MgAl_2O_4$ spinel via modified sol–gel method, *J. Alloys Compd.* **645** (2015) 535–540.
[36] N. Akbar, M. Javed, A. Arif Khan, A. Masood, N. Ahmed, R.Y. Mehmood, S.N. Khisro, M.A.S. Abdul, M.A.S. Mohammad Haniff, A. Shah, Zircon-type $CaCrO_4$ chromite nanoparticles: synthesis, characterization, and photocatalytic application for sunlight-induced degradation of rhodamine B, *ACS Omega* **8** (2023) 30095–30108.
[37] M. Javed, A.A. Khan, N. Akbar, J. Kazmi, A. Dar, M.A. Mohamed, Low-temperature dielectric relaxation mechanism and correlated barrier hopping transport in neodymium perovskite chromite, *Mater. Res. Bull.* **165** (2023) 112303.
[38] M. Javed, N. Akbar, A.A. Khan, E. Alsubhe, S. Mohammad Alghamdi, H. Karamti, O.A. Albeydani, S. ben Ahmed, J. Kazmi, S.N. Khisro, M.A. Mohamed, Photocatalytic activity of sol-gel self-combustion derived MCr_2O_4 (M= Mg, Ni) spinel chromites for photodegradation of organic dyes, *Mater. Today Commun.* **35** (2023) 105716.
[39] F. Li, Y. Zhao, Y. Liu, Y. Hao, R. Liu, D. Zhao, Solution combustion synthesis and visible light-induced photocatalytic activity of mixed amorphous and crystalline $MgAl_2O_4$ nanopowders, *Chem. Eng. J.* **173** (2011) 750–759.
[40] S. Banerjee, S. Mukherjee, S.R. Ghosh, Evaluation of properties of non-stoichometric alumina magnesia spinel using thiourea as fuel by varying soaking time, *J. Eng. Res.* **18** (2021) 44–51.
[41] M. Javed, A.A. Khan, S.N. Khisro, A. Majeed, J. Kazmi, R. Bilkees, M. Hussain, M.A. Mohamed, Charge conduction mechanism and non-debye type relaxation in $LaCrO_3$ perovskite orthochromite, *Mater. Chem. Phys.* **290** (2022) 126522.
[42] M. Javed, A. Arif Khan, J. Kazmi, N. Akbar, N. Ahmed, S.N. Khisro, M.A. Mohamed, Investigation on electrical transport and dielectric relaxation mechanism in $TbCrO_3$ perovskite orthochromite, *J. Alloys Compd.* **955** (2023) 170181.
[43] M.Y. Nassar, I.S. Ahmed, I. Samir, A novel synthetic route for magnesium aluminate ($MgAl_2O_4$) nanoparticles using sol–gel auto combustion method and their photocatalytic properties, *Spectrochim. Acta A Mol. Biomol. Spectrosc.* **131** (2014) 329–334.
[44] E.M.M. Ewais, A.A.M. El-Amir, D.H.A. Besisa, M. Esmat, B.E.H. El-Anadouli, Synthesis of nanocrystalline $MgO/MgAl_2O_4$ spinel powders from industrial wastes, *J. Alloys Compd.* **691** (2017) 822–833.
[45] B. Goswami, N. Rani, R. Vats, C. Bhukkal, R. Ahlawat, Highly crystalline and narrow bandgap $MgAl_2O_4$: synthesis and characterization, *AIP Conference Proceedings, AIP Publishing*, (2021) p. 020045.
[46] E. Abbasi Asl, M. Haghighi, A. Talati, Enhanced simulated sunlight-driven magnetic $MgAl_2O_4$-AC nanophotocatalyst for efficient degradation of organic dyes, *Sep. Purif. Technol.* **251** (2020) 117003.
[47] M. Kaur, K. Pal, Review on hydrogen storage materials and methods from an electrochemical viewpoint, *J. Energy Storage* **23** (2019) 234–249.
[48] T. Gholami, M. Pirsaheb, Review on effective parameters in electrochemical hydrogen storage, *Int. J. Hydrogen Energy* **46** (2021) 783–795.
[49] F.S. Sangsefidi, M. Salavati-Niasari, Thermal decomposition synthesis, characterization and electrochemical hydrogen storage characteristics of Co_3O_4–CeO_2 porous nanocomposite, *Int. J. Hydrogen Energy* **42** (2017) 20071–20081.
[50] A. Salehabadi, M. Salavati-Niasari, T. Gholami, Green and facial combustion synthesis of $Sr_3Al_2O_6$ nanostructures; a potential electrochemical hydrogen storage material, *J. Clean Prod.* **171** (2018) 1–9.
[51] F. Samimi, M. Ghiyasiyan-Arani, M. Salavati-Niasari, Synthesis of calcium manganese oxide with different constructions as potential materials for electrochemical hydrogen storage, *Fuel* **321** (2022) 124074.
[52] H. Zhu, Y. Cao, J. Zhang, W. Zhang, Y. Xu, J. Guo, W. Yang, J. Liu, One-step preparation of graphene nanosheets via ball milling of graphite and the application in lithium-ion batteries, *J. Mater. Sci.* **51** (2016) 3675–3683.